

Journal Pre-proofs

Nb₂CT_x MXene: High capacity and ultra-long cycle capability for lithium-ion battery by regulation of functional groups

Jiabao Zhao, Jing Wen, Junpeng Xiao, Xinzhi Ma, Jiahui Gao, Lina Bai,
Hong Gao, Xitian Zhang, Zhiguo Zhang

PII: S2095-4956(20)30373-9

DOI: <https://doi.org/10.1016/j.jechem.2020.05.037>

Reference: JECHEM 1345



To appear in: *Journal of Energy Chemistry*

Received Date: 27 April 2020

Revised Date: 14 May 2020

Accepted Date: 15 May 2020

Please cite this article as: J. Zhao, J. Wen, J. Xiao, X. Ma, J. Gao, L. Bai, H. Gao, X. Zhang, Z. Zhang, Nb₂CT_x MXene: High capacity and ultra-long cycle capability for lithium-ion battery by regulation of functional groups, *Journal of Energy Chemistry* (2020), doi: <https://doi.org/10.1016/j.jechem.2020.05.037>

This is a PDF file of an article that has undergone enhancements after acceptance, such as the addition of a cover page and metadata, and formatting for readability, but it is not yet the definitive version of record. This version will undergo additional copyediting, typesetting and review before it is published in its final form, but we are providing this version to give early visibility of the article. Please note that, during the production process, errors may be discovered which could affect the content, and all legal disclaimers that apply to the journal pertain.

© 2020 Published by ELSEVIER B.V. and Science Press on behalf of Science Press and Dalian Institute of Chemical Physics, Chinese Academy of Sciences.

Nb₂CT_x MXene: High capacity and ultra-long cycle capability for lithium-ion battery by regulation of functional groups

Jiabao Zhao^a, Jing Wen^a, Junpeng Xiao^a, Xinzhi Ma^a, Jiahui Gao^a, Lina Bai^a, Hong Gao^{a,*}, Xitian Zhang^a, Zhiguo Zhang^b

^a Key Laboratory for Photonic and Electronic Bandgap Materials, Ministry of Education, School of Physics and Electronic Engineering, Harbin Normal University, Harbin 150025, Heilongjiang, China

^b School of Instrumentation Science and Engineering, Harbin Institute of Technology, Harbin 150001, Heilongjiang, China

*Corresponding author.

E-mail address: gaozhong65cn@126.com (H. Gao).

ABSTRACT

MXenes are well known for their potential application in supercapacitors due to their high-rate intercalation pseudocapacitance and long cyclability. However, the reported low capacity of pristine MXenes hinders their practical application in lithium-ion batteries. In this work, a robust strategy is developed to control the functional groups of Nb₂CT_x MXene. The capacity of pristine Nb₂CT_x MXene can be significantly increased by Li⁺ intercalation and surface modification. The specific capacity of the treated Nb₂CT_x is up to 448 mAh g⁻¹ at 0.05 A g⁻¹, and at a large current density of 2 A g⁻¹ remains a high reversible capacity retention rate of 75% after an ultra-long cycle of 2000 cycles. These values exceed most of the reported pristine MXenes (including the most studied Ti₃C₂T_x) and carbon-based materials. It demonstrates that this strategy has great help to improve the electrochemical performance of pristine

MXene, and the results enhance the promise of MXenes in the application of lithium-ion batteries.

Keywords: MXene; Nb₂CT_x; Functional groups; Lithium-ion batteries

1. Introduction

High-capacity lithium-ion batteries are getting unprecedented attention due to their potential to storage the natural energy to relieve the problems of deficiency in traditional fossil fuels and environmental pollution [1–3]. The anode material is an important part of lithium-ion batteries, but the widely used graphite can't meet the high-capacity and high-rate requirements of industrial society, and the candidates are still underdeveloped [4–6]. MXenes [7–9], as a new type of two-dimensional early transition metal carbide and carbonitride, have exhibited excellent electrochemical performance and superior kinetics as an anode material, and has received extensive attention in recent years [10–12]. MXenes can be exfoliated from the three-dimensional (3D) layered MAX phases under hydrofluoric acid aqueous solution (HF) or in situ HF (e.g. hydrochloric acid (HCl) and fluoride) with the general formula M_{n+1}AX_n ($n=1\text{--}3$), where M represents an early transition metal, A is III or IV A-group elements, and X is carbon and/or nitrogen [13]. During the exfoliation process, the layer A of the MAX phase is etched such that the layered M_{n+1}X_n can carry the functional groups (−OH, −O, −F groups) on the surfaces, which can be denoted by M_{n+1}X_nT_x (T_x represents surface functional groups). So far, MXenes have been used in many fields, such as energy storage, photocatalysis and electrocatalysis, hydrogen storage, electromagnetic interference shielding and sewage

purification. In particular, the field of energy storage, such as batteries and supercapacitors [14,15], has received more and more attention in recent years. Among MXene materials, more atomic layers in each formula unit have larger molecular mass, which limits its specific capacity. Therefore, the M_2X structure has a higher specific capacity compared to its M_3X_2 and M_4X_3 counterparts [16]. Nb_2CT_x , one of MXenes with M_2X structure, has attracted more and more attention due to the advantages of high theoretical specific capacity (542 mAh g^{-1}), fast ion movement with very low diffusion barrier heights ($< 0.1 \text{ eV}$) and lower average intercalation potentials [17]. Since Nb_2CT_x MXene was first prepared in 2013 [18], most of the research was about the application of Nb_2CT_x in the field of energy storage. However, the gap between actual specific capacity and theoretical specific capacity is large. Therefore, it is a challenge to further improve the specific capacity and cyclic stability of Nb_2CT_x . Theoretical research shows that the functional groups have a great influence on the electrochemical properties of MXene [19]. Xie et al. combined density functional theory and experiments to determine the relationship between surface structure and Li^+ storage performance [20]. Studies have shown that the $-F/-OH$ group is sensitive to the adsorption of Li, leading to surface instability, and the larger $-OH$ groups will have a higher barrier to Li migration during lithiation [21]. However, compared with the $-OH$ terminated/ $-F$ terminated/bare MXenes, the adsorption energy of the $-O$ terminated MXenes is lower, indicating the highest theoretical Li^+ storage capacity due to the adsorption of more Li atoms [20]. So increasing the content of $-O$ functional group is one of the main directions to improve

the energy storage performance of MXene. Some work on $Ti_3C_2T_x$ has shown that the use of K^+ embedding, annealing, and other methods will affect the functional groups of the system [22,23], but there is no experimental report on Nb_2CT_x MXene in this field.

To solve the above problems, we design a simple and effective scheme to regulate the surface functional groups of Nb_2CT_x to expect better electrochemical properties. Firstly, pristine Nb_2CT_x is subjected to LiOH solution to introduce more oxygen-containing functional groups. In the second step, the obtained Li^+ intercalation Nb_2CT_x is annealed at different temperatures to quantitatively change the content of surface functional groups ($-OH$, $-O$, $-F$). The effects of different kinds of functional groups on electrochemical properties of Nb_2CT_x are clarified and the Li storage capacity and dynamics of the modified Nb_2CT_x MXene are analyzed. The results show that the pre-intercalation of Li^+ and annealing could effectively modify Nb_2CT_x MXene. The specific capacity of this electrode material is as high as 448 $mAh\ g^{-1}$ at a current density of $0.05\ A\ g^{-1}$, which is higher than that of $Ti_3C_2T_x$ electrodes [24] and is by far the highest value among the reported Nb_2CT_x materials. In addition, at a high current density of $2\ A\ g^{-1}$, the electrode material is able to maintain a high specific capacity of $342\ mAh\ g^{-1}$ after an ultra-long cycle of 2000 cycles. And the reversible capacity retention rate is as high as 75%, which demonstrates that it has stable cycle performance.

2. Experimental

2.1. Synthesis of Nb_2CT_x MXene

Nb_2CT_x was synthesized by etching 1 g Nb_2AlC powder (~400 mesh) with HF acid aqueous solution (50% conc.) at room temperature for 240 h under consecutive stirring. After that, the mixture was washed by the centrifugal machine at 8000 rpm until the pH of the supernatant reached around 5. The precipitate was collected by vacuum filtration and put into the vacuum drying oven, drying at 60 °C for 12 h.

2.2. Post-treatment of Nb_2CT_x MXene

Nb_2CT_x samples were post-treated using 1 M LiOH solution (1 g Nb_2CT_x per 100 mL of aqueous LiOH solution) and stirred for 24 h, respectively. The mixture was then washed by ultrapure water several times and desiccated. The obtained cation-intercalation Nb_2CT_x was then annealed at 200 °C, 300 °C, 400 °C and 500 °C for 2 h in H₂/Ar atmosphere, respectively.

2.3. Material characterization

X-ray diffraction (XRD, D/max 2600, Rigaku, Japan) was used to characterize the crystal structure of the samples. Scanning electron microscopy (SEM, SU70, Hitachi, Japan) equipped with an energy-dispersive X-ray spectroscopy (EDS) were used to characterize the micromorphologies and element composition of the samples. Fourier transform infrared spectrometer (FT-IR spectra were obtained using a Magna Model 560 FT-IR spectrometer with a resolution of 1 cm⁻¹) was used to determine the structural information. The element composition of the samples was analyzed by an X-ray photoelectron spectroscopy (XPS, K-alpha X-ray spectrometer, Thermo Scientific Company).

2.4. Assembly of half-cell

The working electrode consists of the active material, conductive auxiliary agent (acetylene black) and the PVDF in a weight ratio of 7:2:1. And then the material was uniformly coated on the copper foil with a doctor blade, and the copper foil was baked in a vacuum drying oven at 60 °C for 24 h to remove moisture. The electrolyte in the battery was a mixed solution of ethylene carbonate/dimethyl carbonate/ethylmethyl carbonate (EC/DEMC/EMC) solvent (volume ratio of EC/DMC/EMC = 1/1/1). The CR2016 coin cells were used for electrochemical testing. The assembly of the CR2016 coin cells was carried out in an argon-filled glove box (MBRAUN UNIlab Plus) with a water and oxygen content of less than 0.5 ppm.

2.5. Electrochemical measurement

The charge and discharge processes were tested in the LAND-2100 automatic battery tester with a voltage range of 0.01~3 V. Cyclic voltammetry testing was performed using Bio-Logic's VSP electrochemical workstation, and the voltage sweep rate tested by cyclic voltammetry was 0.5 m V S⁻¹. All electrochemical tests were performed at room temperature.

3. Results and discussion

The different post-treated Nb₂CT_x samples are named as Li-Nb₂CT_x, Li-Nb₂CT_x-200, Li-Nb₂CT_x-300, Li-Nb₂CT_x-400, and Li-Nb₂CT_x-500, respectively, where the prefix denotes Li⁺ intercalation and the postfix denotes the annealing temperature. For comparison, the pristine Nb₂CT_x was also annealed at 400 °C, named as Nb₂CT_x-400. The significant procedures and features of HF etching, Li⁺ intercalation, and annealing of the samples are summarized in Fig. 1.

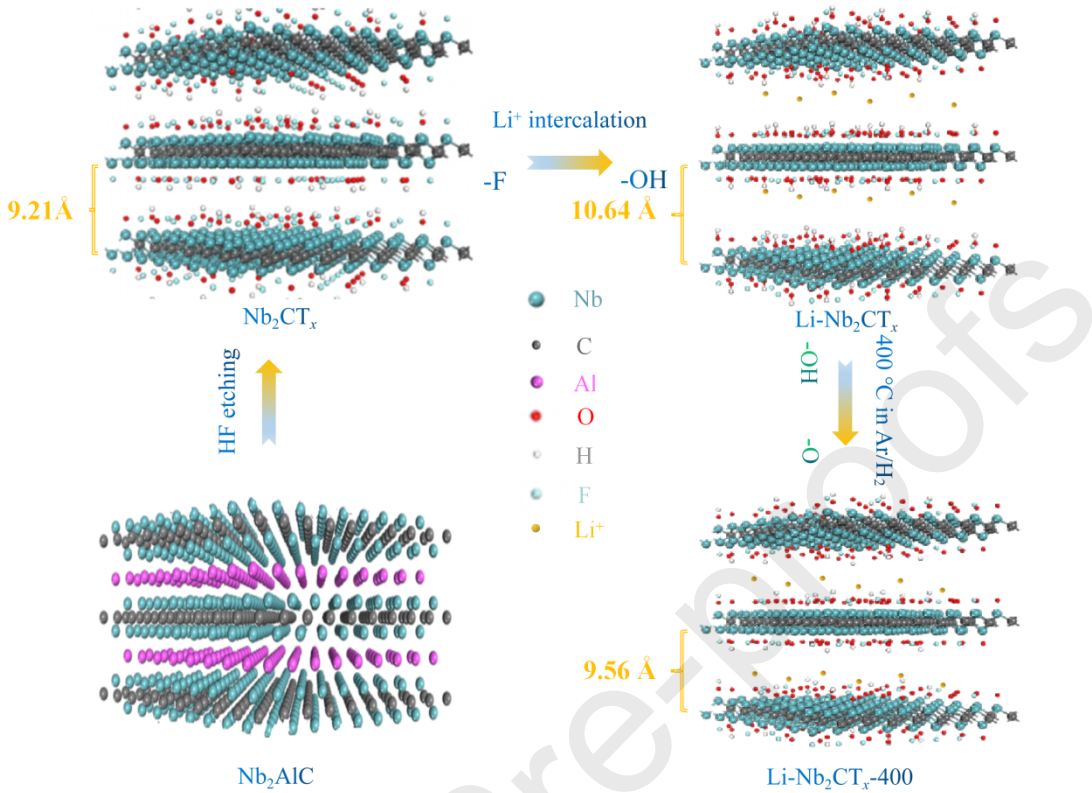


Fig. 1. Schematic illustration of etching, intercalation, and annealing procedures.

3.1. Characterization analysis of various Nb_2CT_x samples

The crystalline structures of Li^+ intercalation and annealed Nb_2CT_x were characterized by XRD. As shown in Fig. 2(a), the (002) peak of the pristine Nb_2CT_x centers at 9.6° and the interlayer spacing is computed to be approximately 9.2 Å. The characteristic peak of Nb_2AlC (38.9°) disappears after etching, which proves that Nb_2CT_x MXene is successfully prepared. After treated with LiOH, the interlayer spacing of Nb_2CT_x increases from 9.2 to 10.6 Å. The interlayer spacing of 10.6 Å could be ascribed to the co-intercalation of water molecules and Li^+ . This feature has also been confirmed by many reported results in different MXenes [22,25]. The (002) peaks are shifted to large angles after $\text{Li}-\text{Nb}_2\text{CT}_x$ being annealed (Fig. 2b), and the

interlayer spacings decrease to about 9.6 Å. The change in interlayer spacing of Li-Nb₂CT_x after annealing is due to the removal of water between the layers [22,26], and compared with the pristine Nb₂CT_x, the increase of interlayer spacing after annealing proves the successful intercalation of Li⁺.

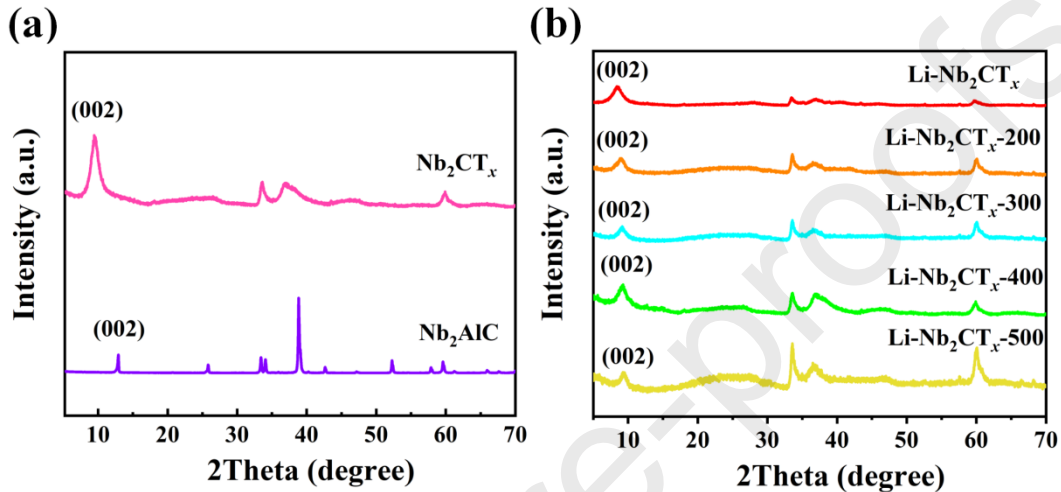


Fig. 2. XRD of (a) Nb₂CT_x and Nb₂AlC, and (b) Li-Nb₂CT_x, Li-Nb₂CT_x-200, Li-Nb₂CT_x-300, Li-Nb₂CT_x-400 and Li-Nb₂CT_x-500.

The SEM images of different Nb₂CT_x samples are shown in Fig. 3. The pristine Nb₂CT_x has a clear layered structure with a clean surface (Fig. 3a). After Li⁺ intercalation, the layered structure of Nb₂CT_x MXene can be well maintained and verified by the SEM images (Fig. 3b). Meanwhile, the SEM images of the samples annealed at different temperatures are shown in Fig. 3(c)-(f). Li-Nb₂CT_x-200, Li-Nb₂CT_x-300, Li-Nb₂CT_x-400 and Li-Nb₂CT_x-500 all maintain a good layered structure.

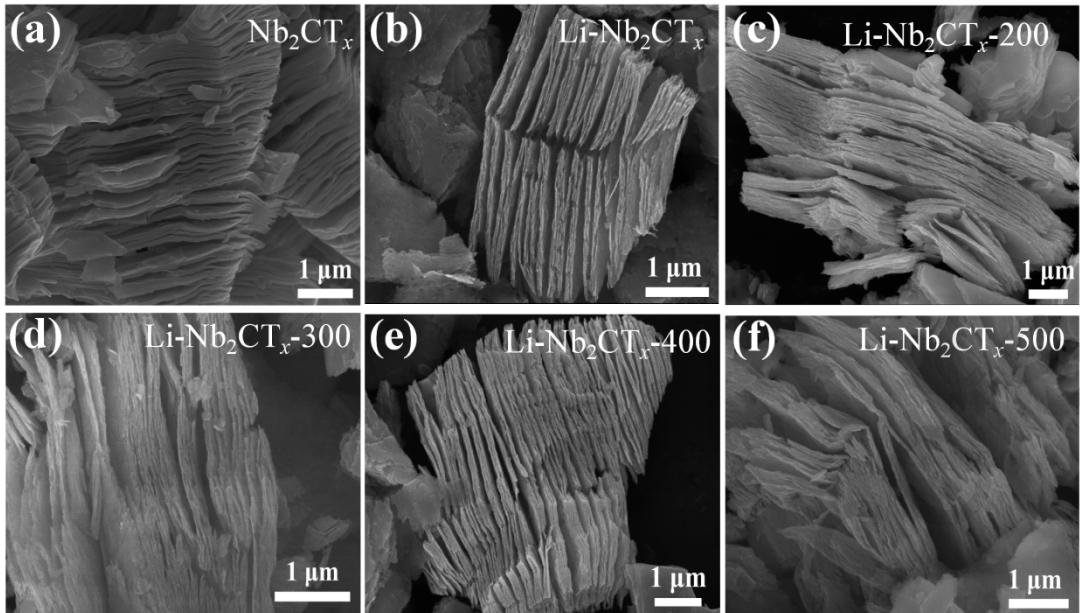


Fig. 3. SEM images of (a) Nb_2CT_x , (b) $\text{Li-Nb}_2\text{CT}_x$, (c) $\text{Li-Nb}_2\text{CT}_x\text{-}200$, (d) $\text{Li-Nb}_2\text{CT}_x\text{-}300$, (e) $\text{Li-Nb}_2\text{CT}_x\text{-}400$, and (f) $\text{Li-Nb}_2\text{CT}_x\text{-}500$.

Stoichiometric ratios of the samples were evaluated by analyzing the EDS data. Fig. 4 shows EDS histograms of the atomic ratio of O and F to Nb of various Nb_2CT_x samples. It can be seen from Fig. 4 that the ratio of O to Nb and F to Nb changed after Li^+ intercalation. The ratio of O to Nb in Nb_2CT_x and $\text{Li-Nb}_2\text{CT}_x$ is 0.20:1 and 0.42:1, the ratio of F to Nb is 0.16:1 and 0.04:1, respectively, indicating an increasing trend of O-containing groups and decreasing of $-\text{F}$ groups because of Li^+ intercalation. The reason for the different proportions is that $-\text{F}$ functional group on the surface of the Nb_2CT_x can be replaced by $-\text{OH}$ after LiOH solution treatment due to the instability of the Nb-F bond in an alkaline solution [27]. It has been further confirmed by XPS spectrum as discussed below. The EDS ratios of the annealed $\text{Li-Nb}_2\text{CT}_x$ showed that the content of $-\text{F}$ functional group further reduced significantly and O-containing

functional group increased when the annealing temperature reaches 400 °C. These results indicate that the annealing process with an optimal temperature can effectively control the surface functional groups.

But we can't identify the existing state of O-containing groups by EDS, which needs further confirmation by FT-IR spectroscopy and XPS.

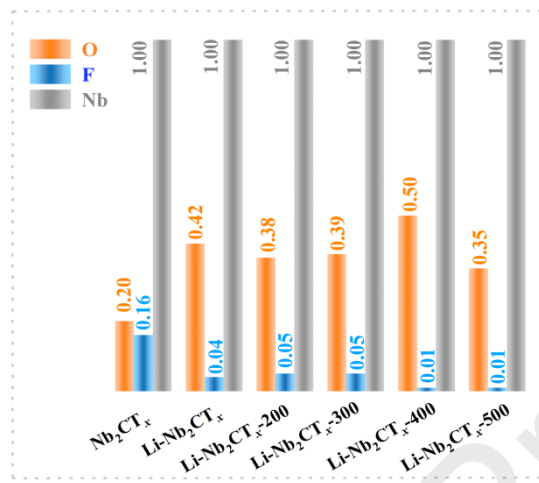


Fig. 4. EDS histograms of the atomic ratio of O and F to Nb in Nb_2CT_x , $\text{Li}-\text{Nb}_2\text{CT}_x$, $\text{Li}-\text{Nb}_2\text{CT}_x-200$, $\text{Li}-\text{Nb}_2\text{CT}_x-300$, $\text{Li}-\text{Nb}_2\text{CT}_x-400$, and $\text{Li}-\text{Nb}_2\text{CT}_x-500$.

From the FT-IR results shown in Fig. 5, the composition of the surface functional groups of the materials can be identified. The broad peak at 3419 cm^{-1} and the sharp peaks at 1385 and 1475 cm^{-1} of all samples are attributed to the tensile vibration and deformation vibration of O-H, respectively [28–30]. The peaks at 1051 , 1091 and 1639 cm^{-1} can be attributed to the stretching vibration of C-O, C-F and C=O, respectively [31]. Therefore, we can conclude that the groups including –O, –OH and –F exist on the pristine Nb_2CT_x and modified Nb_2CT_x surfaces with different ratios remain undetermined.

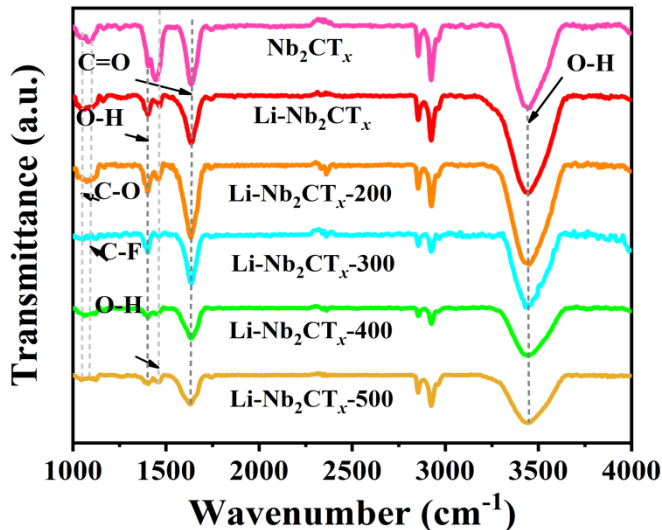


Fig. 5. FT-IR spectroscopy of Nb_2CT_x , $\text{Li-Nb}_2\text{CT}_x$, $\text{Li-Nb}_2\text{CT}_x\text{-}200$, $\text{Li-Nb}_2\text{CT}_x\text{-}300$, $\text{Li-Nb}_2\text{CT}_x\text{-}400$ and $\text{Li-Nb}_2\text{CT}_x\text{-}500$.

3.2. Quantitative analysis of the functional groups

To analyze quantitatively the ratios of $-\text{O}$, $-\text{OH}$, $-\text{F}$ functional groups at different annealing temperatures, we performed XPS testing on all of the samples. Their chemical states (Table S1, S2) are gained from respective high-resolution XPS spectra. The XPS survey scans of Nb_2CT_x , $\text{Li-Nb}_2\text{CT}_x$ and $\text{Li-Nb}_2\text{CT}_x\text{-}400$ are shown in Fig. 6(a). O⁻ and F⁻ high-resolution spectrums are shown in Fig. 6(b) and (c), respectively. The results of XPS analysis of other samples are shown in Fig. S1. The Li 1s spectrum of Nb_2CT_x and $\text{Li-Nb}_2\text{CT}_x$ are shown in Fig. S2, which proves the existence of Li^+ (Fig. S2b). The contents of the $-\text{O}$, $-\text{OH}$ and $-\text{F}$ functional groups are evaluated based on the high-resolution XPS spectra of the samples (see Tables S3, S4). The results are listed in Fig. 7.

After LiOH solution treatment, the content of $-\text{OH}$ and $-\text{F}$ functional groups changed significantly, $-\text{OH}$ from 6.5% to 12.4%, $-\text{F}$ from 10.6% to 3.2%,

respectively. And the content of $-O$ functional group remains almost the same, 14.8% for Nb_2CT_x and 15.6% for $Li-Nb_2CT_x$, respectively. This is because the $-F$ functional group on the surface of the sample is unstable in alkaline solution and is easily replaced by the $-OH$ functional group. As shown in Fig. 6(d), LiF appeared at 685.5 eV [32], the theoretical calculation shows that while intercalating with alkali metal ions, the $-F$ functional group is unstable and has a chance to form metal fluoride [26], leading to some decrease of $-F$ groups.

After $Li-Nb_2CT_x$ is annealed at different temperatures, the content of $-O$, $-OH$ and $-F$ functional groups of the samples are all regulated further. The contents of $-O$ functional groups in the samples of $Li-Nb_2CT_x$, $Li-Nb_2CT_x-200$, $Li-Nb_2CT_x-300$, $Li-Nb_2CT_x-400$ and $Li-Nb_2CT_x-500$ are 15.6%, 15.6%, 17.7%, 28.5%, and 20.7%, respectively. The content of $-OH$ functional groups are 12.4%, 12.4%, 10.3%, 2.6%, and 2.6%, respectively. It can be seen that the content of $-O$ functional group in $Li-Nb_2CT_x-400$ is nearly double that in $Li-Nb_2CT_x$, while the content of $-OH$ functional group is less than 1/5 of that in $Li-Nb_2CT_x$. The reason is that based on the surface structures after HF etching, the following high-temperature reactions were considered [20]:



After annealing in Ar/H_2 atmosphere, the content of $-F$ functional groups also decrease, and the ratios were 3.2%, 3.2%, 2.6%, 0.7%, and 0.7%, respectively. The reason for the decrease is that hydrogen can react with the $-F$ functional group and

the resultants could flow away at a certain temperature. At the same time, we found that after the sample is annealed at 500 °C, the content of NbO_x in the sample is higher than that of Li-Nb₂CT_x-400 (Table S3), which suggests that the degree of oxidation of Li-Nb₂CT_x-500 is higher than that of Li-Nb₂CT_x-400 and 500 °C is not a preferred annealing temperature in this work. The data of XPS here is consistent with that of EDS.

To explore the modulation effect and mechanism of Li⁺ intercalation and annealing on functional groups and interlayer spacing, the structure and composition of Nb₂CT_x annealed at 400 °C without Li⁺ intercalation were also characterized. For pristine Nb₂CT_x, after annealing at 400 °C, we found that the interlayer spacing decrease to 7.6 Å (Fig. S3a), the –O, –F and –OH functional groups contents are 20.2%, 3.1%, 2.7%, respectively (Tables S3, S4). The interlayer spacing of Li-Nb₂CT_x-400 is 2.0 Å larger than that of Nb₂CT_x-400. This indicates that Li⁺ has a function of fixing interlayer spacing, which to some extent prevents the reduction of interlayer spacing caused by the water molecule escaping during the annealing process, thus facilitating the storage of more Li⁺. The content of –O functional group in Li-Nb₂CT_x-400 is more than that in Nb₂CT_x-400 by nearly 1/3, while the content of –F is less than a quarter. It indicates that with the help of Li⁺ intercalation, –OH functional group replaces –F functional group first, and then by annealing, the –O can be increased and –F be decreased more effectively. The cooperative treatment strategy of Li⁺ intercalation and annealing can greatly improve Li⁺ storage capacity of the electrode materials.

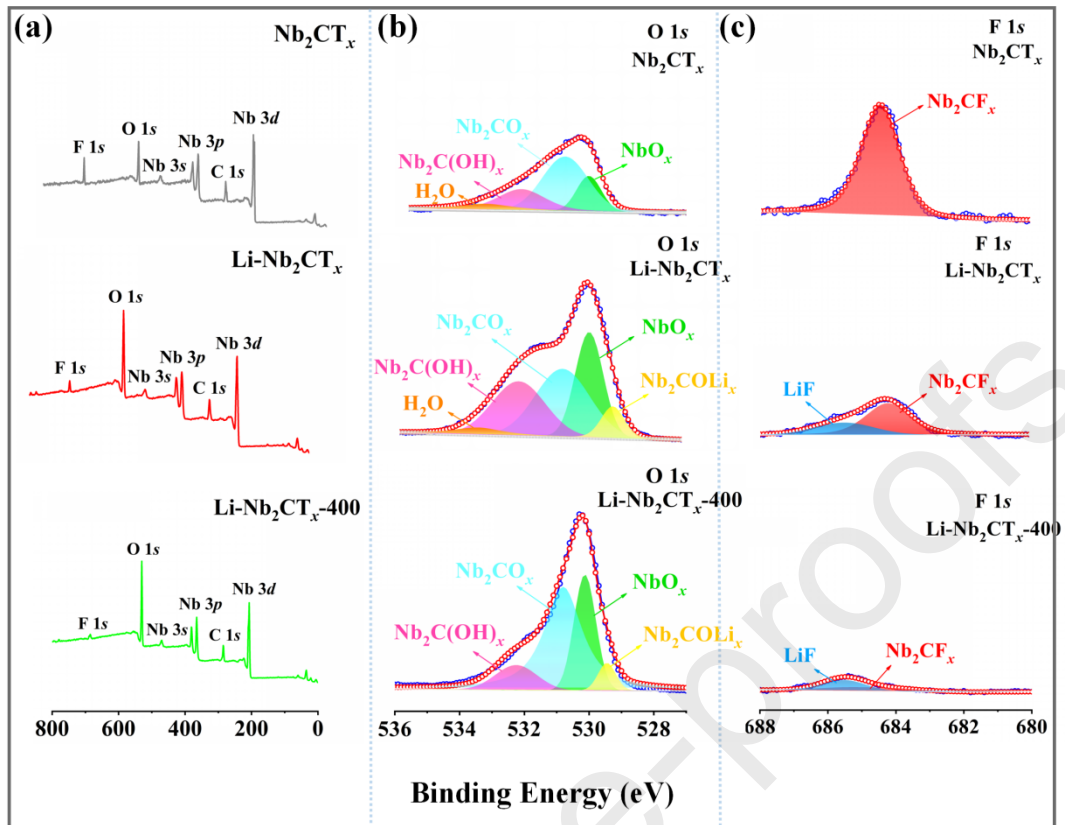


Fig. 6. (a) Survey XPS spectra, (b) O 1s spectra, (c) F 1s spectra of Nb_2CT_x , $\text{Li}-\text{Nb}_2\text{CT}_x$ and $\text{Li}-\text{Nb}_2\text{CT}_x-400$.

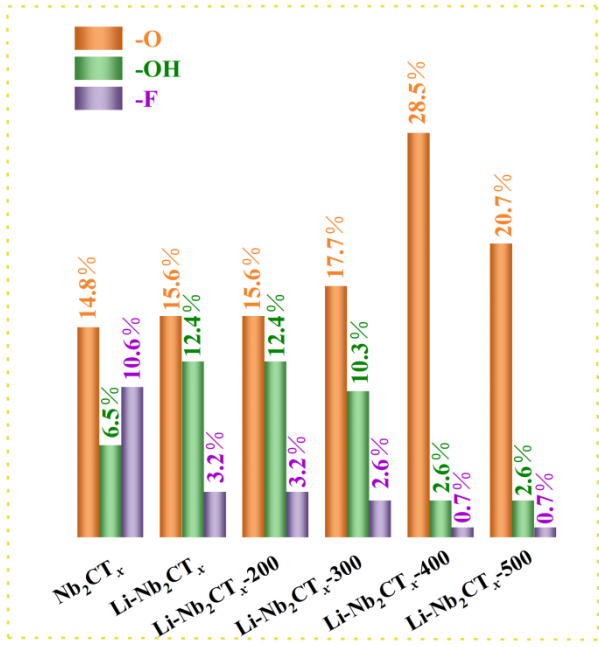


Fig. 7. The content of $-\text{O}$, $-\text{OH}$, and $-\text{F}$ functional groups of various Nb_2CT_x samples.

3.3. Electrochemical performance of various Nb_2CT_x samples

To test the effect of functional groups and Li^+ intercalation on electrochemical properties, electrode materials prepared from pristine Nb_2CT_x and modified Nb_2CT_x were assembled into CR2016 coin cells to compare their electrochemical properties as lithium-ion batteries.

CV curves at a rate of 0.5 mV s^{-1} for $\text{Li-Nb}_2\text{CT}_x\text{-}400$ are shown in Fig. 8(a). The CV profiles of other different treatment of Nb_2CT_x materials look quite similar to that of the $\text{Li-Nb}_2\text{CT}_x\text{-}400$ electrode (Fig. S4). In the test results of the first circle, there are two reduction peaks near 0.63 and 1.51 V. The irreversible peak at 0.63 V is derived from the solid interface film (SEI) on the surface of the electrode [33]. In the subsequent cycle, broadened oxidation peaks appear at 0.69 and 1.75 V, which corresponded to the intercalation and deintercalation of Li^+/Li between the MXene layers. From the second cycle, the shape of the CV curve remains essentially

unchanged, indicating that the Li^+ is reversible in the material's embedding process.

Fig. 8(b) shows the GDC curve of the first cycle of pristine Nb_2CT_x and modified Nb_2CT_x electrodes at 0.05 A g^{-1} . The first discharge and charging capacity of $\text{Li-Nb}_2\text{CT}_x\text{-}400$ electrode are 985 and 623 mAh g^{-1} , respectively, which is the highest among all modified materials, and its initial coulomb efficiency is 63.2% . The first cycle irreversibility may be partly due to the expected formation of SEI [34].

From Fig. 8(c), at a current density of 0.05 A g^{-1} , the specific capacity of the pristine Nb_2CT_x and $\text{Li-Nb}_2\text{CT}_x$ are 159 and 300 mAh g^{-1} after 50 cycles, respectively. After the intercalation of Li ions, the electrochemical performance of Nb_2CT_x has been improved greatly. The specific capacity of $\text{Li-Nb}_2\text{CT}_x\text{-}400$ is 448 mAh g^{-1} , which is higher than that of $\text{Li-Nb}_2\text{CT}_x$ annealed at other temperatures. It is noteworthy that the specific capacity of $\text{Li-Nb}_2\text{CT}_x\text{-}500$ is lower than that of $\text{Li-Nb}_2\text{CT}_x\text{-}400$. The reason is that the degree of oxidation in $\text{Li-Nb}_2\text{CT}_x\text{-}500$ is higher than that in $\text{Li-Nb}_2\text{CT}_x\text{-}400$, and the content of $-\text{O}$ functional group in $\text{Li-Nb}_2\text{CT}_x\text{-}500$ (20.7%) is lower than that in $\text{Li-Nb}_2\text{CT}_x\text{-}400$ (28.5%) in the XPS test (Fig. 7). Furthermore, these electrodes all show excellent cycling stability with a Coulomb efficiency close to 100% (Fig. S5). Meanwhile, the rate capability is a key indicator for the large-scale application of energy storage devices. $\text{Li-Nb}_2\text{CT}_x\text{-}400$ exhibits stable and durable capacity at different current densities ($0.05\text{--}2 \text{ A g}^{-1}$) and decreases as current density increases (Fig. 8d). When the current density is restored from 2 to 0.05 A g^{-1} , the high reversible specific capacity of 450 mAh g^{-1} can be recovered. At the same time, the ultra-long cycle stability of $\text{Li-Nb}_2\text{CT}_x\text{-}400$ electrode under a high

current density of 2 A g^{-1} was tested. After the ultra-long cycle of 2000 cycles, high reversible capacity retention of 75% (342 mAh g^{-1}) is maintained (Fig. 8e). The excellent electrochemical performance of Li-Nb₂CT_x-400 electrode depends on the following points:

The interlayer spacing of the samples increased after Li⁺ intercalation, which accommodates more Li⁺ entering the interlayer. Meanwhile, the intercalation of Li⁺ can effectively increase Li storage site and enhance the storage dynamics of Li. After annealing at 400 °C, the surface of Li-Nb₂CT_x-400 is rich in –O functional group, which can absorb more Li atoms and greatly improve the capacity of Li⁺. While the extremely low contents of –OH and –F benefit the reversibility and cycle stability of Nb₂CT_x anodes [20].

To explore the influence of Li⁺ intercalation on electrochemical performance under annealing at the same temperature, we tested the electrochemical performance of Nb₂CT_x-400 electrode. As shown in Fig. S3(e), at a current density of 0.05 A g^{-1} , the specific capacity of Nb₂CT_x-400 can reach 257 mAh g^{-1} after 50 cycles. After the ultra-long cycle of 2000 cycles, the specific capacity is maintained at 186 mAh g^{-1} , lower than that in Li-Nb₂CT_x-400 (Fig. S3g). This verifies that the intercalation of Li⁺ is significant and is consistent with the previous functional group data.

By analyzing the above electrochemical performance data, the specific capacity of Li-Nb₂CT_x-400 is the best among the pristine and modified Nb₂CT_x. Meanwhile, the specific capacity of Li-Nb₂CT_x-400 is higher than that of Ti₃C₂T_x and the reported Nb₂CT_x electrodes, see Table 1. This reveals that the synergistic effect between Li⁺

intercalation and surface modification is effective in improving the electrochemical performance, which is of great significance to the development of other MXene materials in the field of energy storage.

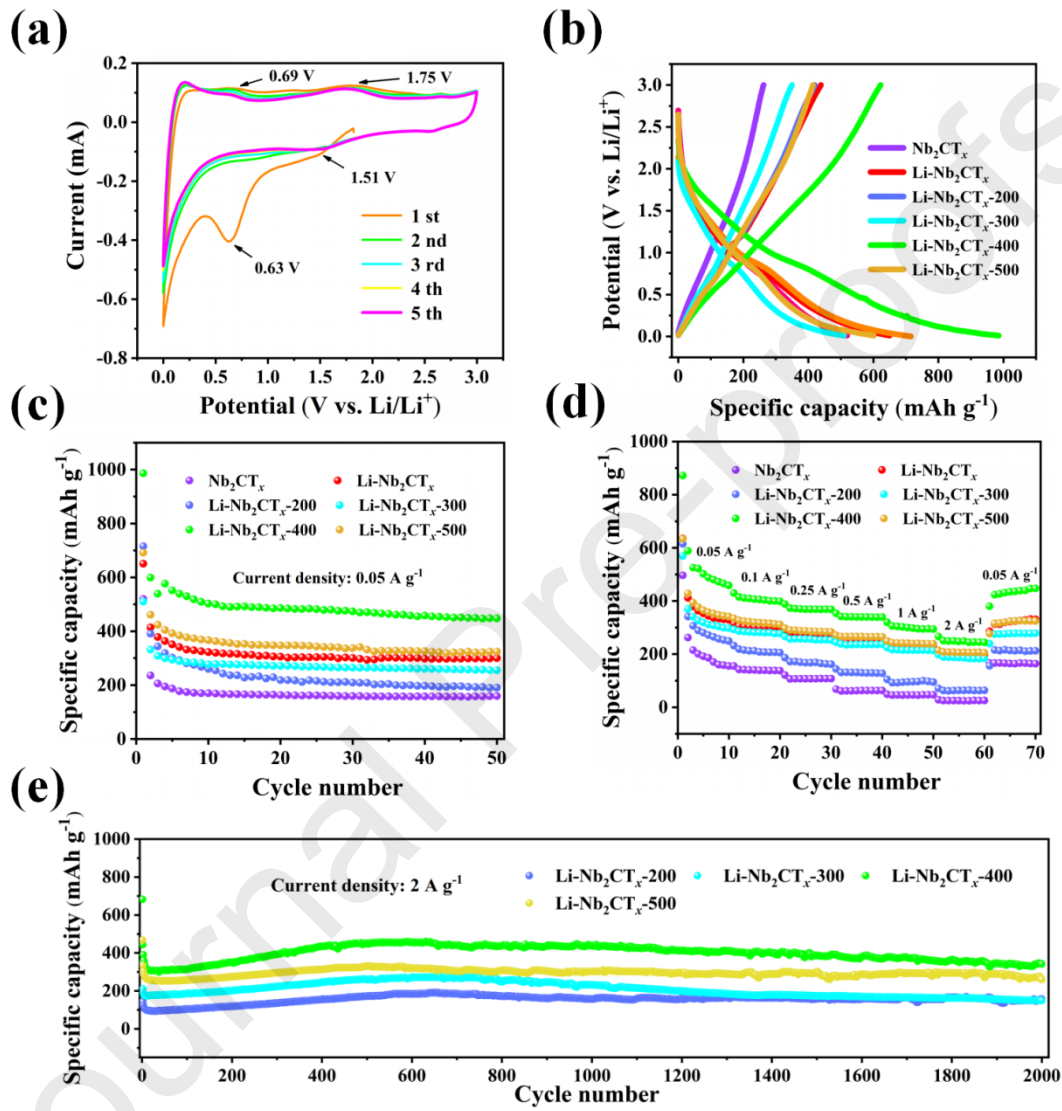


Fig. 8. (a) CV curves of the $\text{Li-Nb}_2\text{CT}_x$ -400 electrode at a scanning rate of 0.5 mV s^{-1} . (b) GDC profiles of the first circle of various Nb_2CT_x electrodes at 0.05 A g^{-1} . (c) Cycling properties at 0.05 A g^{-1} and (d) rate performances at different current densities of various Nb_2CT_x electrodes. (e) Cycling performances of annealed samples at 2.0 A g^{-1} .

Table 1. Comparison of the electrochemical properties of several anode materials.

Sample	Current density	Cycle number	Reversible capacity (mAh g ⁻¹)	Ref.
V ₂ CT _x	1 C	100	280	[18]
Nb ₂ CT _x	1 C	100	170	[18]
Ti ₃ C ₂ -H ₂	100 mA cm ⁻³	100	123.7 mAh cm ⁻³	[19]
Ti ₂ C	1 C	80	110	[35]
Ti ₃ C ₂ T _x	1 C	75	89.7	[36]
Ti ₃ C ₂ T _x after DMSO	1 C	100	123.6	[36]
MoS ₂ /Ti ₃ C ₂	0.5 A g ⁻¹	50	230	[37]
H ₂ O ₂ -Ti ₂ CT _x	0.5 A g ⁻¹	1000	280	[38]
Nb ₂ O ₅ /Nb ₄ C ₃ T _x	0.25 A g ⁻¹	400	208	[39]
Li ₄ Ti ₅ O ₁₂ /Ti ₃ C ₂ T _x	0.5 A g ⁻¹	200	125	[40]
Nb ₄ C ₃ T _x	0.5 A g ⁻¹	100	380	[41]
Nb ₂ CT _x /CNT	0.05 A g ⁻¹	110	300	[42]
Nb ₂ CT _x /CNT	0.5 C	100	420	[43]
Ti ₂ C	10 C	1000	60	[44]
Ti ₂ C	10 C	200	70	[45]
Few-layer Nb ₂ CT _x	0.05 A g ⁻¹	110	354	[46]
ReS ₂	1 A g ⁻¹	500	200	[47]
Li-Nb₂CT_x-400	0.05 A g⁻¹	50	448	This work
	2 A g⁻¹	2000	342	This work

To further explain the improvement of electrochemical performance, the kinetics of Li⁺ storage electrodes (pristine Nb₂CT_x and modified Nb₂CT_x) were analyzed by testing the CV curves at different scanning rates from 0.1 to 2.0 mV s⁻¹ (Fig. 9a-c). In these CV curves, as the scanning rate increases, the redox peak shifts to a higher potential as the peak height increases. In general, the Li⁺ storage mechanism of the pristine Nb₂CT_x and modified Nb₂CT_x electrodes can be quantitatively determined by decomposing the current response *i* at a specific voltage into a capacitance contribution (*k*₁*v*), and diffusion control contribution (*k*₂*v*^{1/2}), based on the relationship between current response and scan rate [48–51].

$$i(v) = k_1 v + k_2 v^{1/2} = av^b \quad (3)$$

Here, *k*₁, *k*₂ and *a* are constants, *v* is the scan rate, and *b* is the tunable range, from 0.5 to 1. The *b* values of 0.5 and 1 represent the process of diffusion-based process and capacitance control, respectively. Calculation results of *a* and *b* (Fig. 9d-f) show the *b*-values of the positive and negative sweeps of Nb₂CT_x, Li-Nb₂CT_x, Li-Nb₂CT_x-400 correspond to 0.95, 0.95, 0.96, 0.96, 0.98, and 0.97, respectively. This result suggests that the fast charge storage capability of Nb₂CT_x, Li-Nb₂CT_x, Li-Nb₂CT_x-400 mainly ascribe to the capacitance contribution. By calculating *k*₁ and *k*₂, the corresponding ratio of current (*i*) for capacitance control and diffusion control can be distinguished. At 2 mV s⁻¹, the contribution ratios of the capacitance control capacitor are 87%, 83%, and 79% for the Li-Nb₂CT_x-400, Li-Nb₂CT_x, and pristine Nb₂CT_x electrode respectively. This phenomenon clearly shows that –O functional group promotes the

storage dynamics of Li^+ and optimizes the kinetics of Li^+ transport between electrolyte and electrode [52]. This is consistent with the changes in previous functional group datum and electrochemical properties.

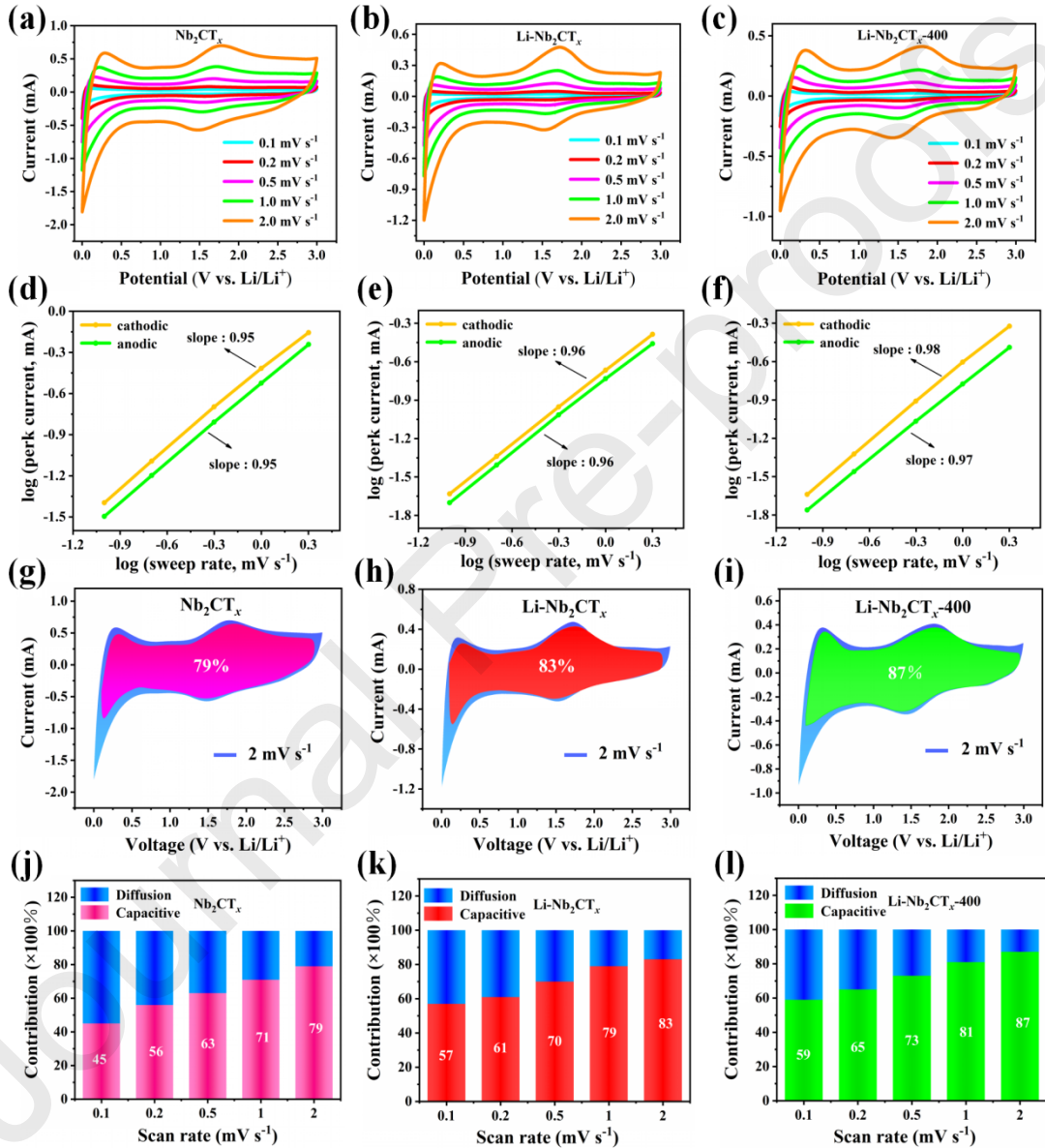


Fig. 9. CV curves of (a) Nb_2CT_x , (b) $\text{Li}-\text{Nb}_2\text{CT}_x$ and (c) $\text{Li}-\text{Nb}_2\text{CT}_x-400$ at various scan rates, b-value determination of the peak currents of (d) Nb_2CT_x , (e) $\text{Li}-\text{Nb}_2\text{CT}_x$ and (f) $\text{Li}-\text{Nb}_2\text{CT}_x-400$. Capacitive and diffusion current contributed to charge storage of (g) Nb_2CT_x , (h) $\text{Li}-\text{Nb}_2\text{CT}_x$ and (i) $\text{Li}-\text{Nb}_2\text{CT}_x-400$, the percentage of capacitance

contribution of (j) Nb_2CT_x , (k) $\text{Li-Nb}_2\text{CT}_x$ and (l) $\text{Li-Nb}_2\text{CT}_x\text{-}400$.

4. Conclusions

A synergistic strategy of intercalation- and termination-engineering has been implemented in Nb_2CT_x MXene and the surface functional groups, and interlayer spacing are effectively regulated. After Li^+ intercalated Nb_2CT_x is annealed at 400 °C, the content of –O functional group increase, while the content of –F and –OH functional groups decrease significantly as expected. Due to the suitable surface functional groups, the electrochemical performance of $\text{Li-Nb}_2\text{CT}_x\text{-}400$ electrode achieves a high specific capacity of 448 mAh g⁻¹ at a current density of 0.05 A g⁻¹ with retention of 75% after 2000 cycles at 2 A g⁻¹. Compared with the reported Nb_2CT_x and $\text{Ti}_3\text{C}_2\text{T}_x$ electrodes, the specific capacity of $\text{Li-Nb}_2\text{CT}_x\text{-}400$ electrode is the highest. The strategy of this work is of great significance for the development of Nb_2CT_x materials in lithium-ion batteries, and it is expected to be applied to other MXene materials.

Acknowledgments

Project supported by the National Science Foundation of China (No.51772070 and 51772069).

References

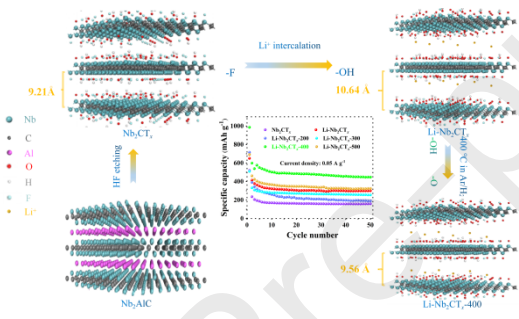
- [1] M. Berecibar, *Nature* 568 (2019) 325–326.
- [2] M. Li, J. Lu, Z.W. Chen and K. Amine, *Adv. Mater.* 30 (2018) 1800561.
- [3] L.N. Cong, H.M. Xie, J.H. Li, *Adv. Energy Mater.* 7 (2017) 1601906.
- [4] E. Pomerantseva, F. Bonaccorso, X.L. Feng, Y. Cui and Y. Gogotsi, *Science* 366 (2019) 969.
- [5] E.Y. Hu, X.L. Wang, X.Q. Yu, and X.Q. Yang, *Acc. Chem. Res.* 51 (2018) 290–298.
- [6] B.W. Xiao and X.L. Sun, *Adv. Energy Mater.* 8 (2018) 1802057.
- [7] Y. Xia, T.S. Mathis, M.Q. Zhao, B. Anasori, A. Dang, Z.H. Zhou, H. Cho, Y. Gogotsi and S. Yang, *Nature* 557 (2018) 409–412.
- [8] M. Naguib, O. Mashtalir, J. Carle, V. Presser, J. Lu, L. Hultman, Y. Gogotsi and M. W. Barsoum, *ACS Nano* 6 (2012) 1322–1331.
- [9] M. Naguib, M. Kurtoglu, V. Presser, J. Lu, J. Niu, M. Heon, L. Hultman, Y. Gogotsi and M. W. Barsoum, *Adv. Mater.* 23 (2011) 4248–4253.
- [10] D.B. Xiong, X.F. Li, Z.M. Bai and S.G. Lu, *Small* 14 (2018) 1703419.
- [11] B. Anasori, M. R. Lukatskaya and Y. Gogotsi, *Nat. Rev. Mater.* 2 (2017) 16098.
- [12] L. Li, J. Wen and X.T. Zhang, *ChemSusChem* 13 (2020) 1296–1329.
- [13] M. Malaki, A. Maleki, R.S. Varma, *J. Mater. Chem. A* 7 (2019) 10843–10857.
- [14] W. Zheng, P. Zhang, J. Chen, W.B. Tian, Y.M. Zhang, Z.M. Sun, *J. Mater. Chem. A* 6 (2018) 3543–3551.
- [15] J.P. Xiao, J. Wen, J.B. Zhao, X.Z. Ma, H. Gao and X.T. Zhang, *Electrochim. Acta* 337 (2020) 135803.
- [16] Y. Xie, Y. Dall’Agnese, M. Naguib, Y. Gogotsi, M. W. Barsoum, H. L. Zhuang, P. R. C. Kent, *ACS Nano* 8 (2014) 9606.
- [17] Y. Luo, C. Cheng, H.-J. Chen, K. Liu and X.L. Zhou, *J. Phys.: Condens. Mat.* 31 (2019) 405703.
- [18] M. Naguib, J. Halim, J. Lu, K. Cook, L. Hultman, Y. Gogotsi and M. W. Barsoum, *J. Am. Chem. Soc.* 135 (2013) 15966–15969.
- [19] M. Lu, H.J. Li, W.J. Han, J.N. Chen, W. Zhang, W.T. Zheng, *J. Energy Chem.* 31 (2019) 148–153.
- [20] Y. Xie, M. Naguib, V. N. Mochalin, M. W. Barsoum, Y. Gogotsi, X. Yu, K. W. Nam, X. Q. Yang, A. I. Kolesnikov and P. R. Kent, *J. Am. Chem. Soc.* 136 (2014) 6385–6394.
- [21] Q. Tang, Z. Zhou and P. Shen, *J. Am. Chem. Soc.* 134 (2012) 16909–16916.
- [22] J. Li, X. T. Yuan, C. Lin, Y. Q. Yang, L. Xu, X. Du, J. L. Xie, J. H. Lin and J. L. Sun, *Adv. Energy Mater.* 7 (2017) 1602725.
- [23] Y.H. Wang, C. Ma, W.Q. Ma, W. F., Y. Sun, H.M. Yin, X.X. Shi, X.Z. Liu and Y. Ding, *2D Mater.* 6 (2019) 045025.
- [24] B.M. Jun, S. Kim, J.Y. Heo, C. M. Park, N. Her, M. Jang, Y. Huang, J.H. Han and Y. Yoon, *Nano Res.* 12 (2019) 471–487.
- [25] J.M. Luo, C. Fang, C.B. Jin, H.D. Yuan, C. Liang, J. Zhang, W.Y. Li, X.Y. Tao,

- J. Mater. Chem. A 6 (2018) 7794–7806.
- [26] J. Wen, X.T. Zhang, H. Gao, Physica B 537 (2018) 155–161.
- [27] Q. Peng, J. Guo, Q. Zhang, J. Xiang, B. Liu, A. Zhou, R. Liu and Y. Tian, J. Am. Chem. Soc. 136 (2014) 4113–4116.
- [28] H.N. Yang, C.K. Zhang, Q.H. Meng, B. Cao, G.Y. Tian, J. Power Sources 431 (2019) 114–124.
- [29] H.B. Wang, J.F. Wang, Y.P. Wu, H.J. Huang, G.Y. Li, X. Zhang, Z.Y. Wang, Appl. Surf. Sci. 384 (2016) 287–293.
- [30] M.M. Hu, Z.J. Li, T. Hu, S.H. Zhu, C. Zhang, X.H. Wang, ACS Nano 10 (2016) 11344–11350.
- [31] P.T. Yan, R.J. Zhang, J. Jia, C. Wu, A.G. Zhou, J. Xu, X.S. Zhang, J. Power Sources 284 (2015) 38–43.
- [32] P. Niehoff, S. Passerini, M. Winter, Langmuir 29 (2013) 5806–5816.
- [33] S. Han, Y. R. Zhao, Y. P. Tang, F. Z. Tan, Y. S. Huang, X. L. Feng and D. Q. Wu, Carbon 81 (2015) 203–209.
- [34] P. Lian, Y. Dong, Z.-S. Wu, S. Zheng, X. Wang, W. Sen, C. Sun, J. Qin, X. Shi, X. Bao, Nano Energy 40 (2017) 1–8.
- [35] M. Naguib, J. Come, B. Dyatkin, V. Presser, P.L. Taberna, P. Simon, M.W. Barsoum, Y. Gogotsi, Electrochim. Commun. 16 (2012) 61–64.
- [36] D.D. Sun, M.S. Wang, Z.Y. Li, G.X. Fan, L.Z. Fan, A.G. Zhou, Electrochim. Commun. 47 (2014) 80–83.
- [37] M. Zhang, R. Guo, Z. Liu, B. Wang, L. Meng, F. Li, T. Li and Y. Luo, J. Alloys Compd. 735 (2018) 1262–1270.
- [38] B. Ahmed, D. H. Anjum, M. N. Hedhili, Y. Gogotsi and H. N. Alshareef, Nanoscale 8 (2016) 7580–7587.
- [39] S. J. Kim, M. Naguib, M. Q. Zhao, C. F. Zhang, H. T. Jung, M. W. Barsoum and Y. Gogotsi, Electrochim. Acta 163 (2015) 246–251.
- [40] C. Shen, Y. Cao, A. Zhou, Q. Hu, G. Qin, Z. Yang, X. Liu and L. Wang, J. Alloys Compd. 735 (2018) 530–535.
- [41] S. Zhao, X. Meng, K. Zhu, F. Du, G. Chen, Y. Wei, Y. Gogotsi and Y. Gao, Energy Storage Mater. 8 (2017) 42–48.
- [42] A. Byeon, A.M. Glushenkov, Y. Gogotsi, J. Power Sources 326 (2016) 686–694.
- [43] O. Mashtalir, M.R. Lukatskaya, M.Q. Zhao, M.W. Barsoum, Y. Gogotsi, Adv. Mater. 27 (2015) 3501–3506.
- [44] J. Come, M. Naguib, Y. Gogotsi, J. Electrochem. Soc. 159 (2012) A1368–A1373.
- [45] X. Tang, X. Guo, W.J. Wu, and G.X Wang, Adv. Energy Mater. 8 (2018) 1801897.
- [46] J.B. Zhao, J. Wen, L.N. Bai, J.P. Xiao, R.D. Zheng, X.Y. Shan, L. Li, H. Gao, X.T. Zhang, Dalton T. 48 (2019) 14433–14439.
- [47] D. Zhang, S. Wang, Y. Ma, S.B. Yang, J Energy Chem. 27 (2018) 128.
- [48] V. Augustyn, J. Come, M. A. Lowe, J. W. Kim, P. L. Taberna, S. H. Tolbert, H. D. Abruna, P. Simon and B. Dunn, Nat. Mater. 12 (2013) 518–522.
- [49] T. Brezesinski, J. Wang, J. Polleux, B. Dunn and S. H. Tolbert, J. Am. Chem. Soc. 131 (2009) 1802–1809.

- [50] P. Simon, Y. Gogotsi and B. Dunn, Science 343 (2014) 1210–1211.
- [51] X. Guo, J.Q. Zhang, J.J. Song, W.J. Wu, H. Liu, G.X. Wang, Energy Storage Mater. 14 (2018) 306.
- [52] Y. X. Yu, Prediction of Mobility, J. Phys. Chem. C 120 (2016) 5288–5296.

Graphic abstract:

A synergistic strategy of intercalation- and termination-engineering has been implemented in Nb_2CT_x MXene and the specific capacity of the pristine Nb_2CT_x has been greatly improved.



Supporting Information

Nb₂CT_x MXene : High Capacity and Ultra-long Cycle Capability for Lithium-Ion Battery by Regulation of Functional Groups

Jiabao Zhao^a, Jing Wen^a, Junpeng Xiao^a, Xinzhi Ma^a, Jiahui Gao^a, Lina Bai^a, Hong Gao^{a,*}, Xitian Zhang^a, Zhiguo Zhang^b

^a Key Laboratory for Photonic and Electronic Bandgap Materials, Ministry of Education, School of Physics and Electronic Engineering, Harbin Normal University, Harbin 150025, Heilongjiang, China

^b School of Instrumentation Science and Engineering, Harbin Institute of Technology, Harbin 150001, Heilongjiang, China

Table S1. XPS peak fitting results for O 1s region of various Nb₂CT_x samples.

Sample	BE [eV]	Assigned to	Reference
Nb₂CT_x	530.10	NbO _x	[1]
	531.00	Nb ₂ CO _x	[2]
	532.30	Nb ₂ C(OH) _x	[3]
	533.50	H ₂ O	[4]
Li-Nb₂CT_x	529.15	Nb ₂ COLi _x	[5]
	529.95	NbO _x	[1]
	530.80	Nb ₂ CO _x	[2]
	532.20	Nb ₂ C(OH) _x	[3]
Li-Nb₂CT_x-200	533.50	H ₂ O	[4]
	529.20	Nb ₂ COLi _x	[5]
	530.00	NbO _x	[1]
	530.80	Nb ₂ CO _x	[2]
Li-Nb₂CT_x-300	532.20	Nb ₂ C(OH) _x	[3]
	529.30	Nb ₂ COLi _x	[5]
	530.10	NbO _x	[1]
	530.80	Nb ₂ CO _x	[2]
Li-Nb₂CT_x-400	532.20	Nb ₂ C(OH) _x	[3]
	529.33	Nb ₂ COLi _x	[5]
	530.13	NbO _x	[1]
	530.80	Nb ₂ CO _x	[2]
Li-Nb₂CT_x-500	532.20	Nb ₂ C(OH) _x	[3]
	529.35	Nb ₂ COLi _x	[5]
	530.17	NbO _x	[1]
	530.80	Nb ₂ CO _x	[2]
Nb₂CT_x-400	532.20	Nb ₂ C(OH) _x	[3]
	530.13	NbO _x	[1]
	530.80	Nb ₂ CO _x	[2]
	532.20	Nb ₂ C(OH) _x	[3]

Table S2. XPS peak fitting results for F 1s region of various Nb₂CT_x samples.

Sample	BE [eV]	Assigned to	Reference
Nb₂CT_x	684.45	Nb ₂ CF _x	[6]
Li-Nb₂CT_x	684.50	Nb ₂ CF _x	[6]
	685.47	LiF	[7]
Li-Nb₂CT_x-200	684.50	Nb ₂ CF _x	[6]
	685.49	LiF	[7]
Li-Nb₂CT_x-300	684.50	Nb ₂ CF _x	[6]
	685.50	LiF	[7]
Li-Nb₂CT_x-400	684.50	Nb ₂ CF _x	[6]
	685.51	LiF	[7]
Li-Nb₂CT_x-500	684.50	Nb ₂ CF _x	[6]
	685.53	LiF	[7]
Nb₂CT_x-400	684.50	Nb ₂ CF _x	[6]

Table S3 shows the content of O element and its constituents in each sample in XPS. The content of -O, -OH, NbO_x, O-Li and H₂O in the table is obtained by quantitative analysis of the area of each peak under O 1s in XPS.

Table S3. The content of O element and its constituents in each sample in XPS.

sample/content	O 1s	-O	-OH	NbO_x	O-Li	H₂O
Nb₂CT_x	29.7%	50.0%	21.8%	21.2%	0.00%	7.0%
Li-Nb₂CT_x	43.8%	35. 6%	28.4%	26.0%	6.1%	4.0%
Li-Nb₂CT_{x-200}	41.8%	37.4%	29.6%	27.9%	5.1%	0.0%
Li-Nb₂CT_{x-300}	45.7%	38.7%	22.5%	30.6%	8.6%	0.0%
Li-Nb₂CT_{x-400}	47.5%	60.0%	5.5%	29.5%	5.0%	0.0%
Li-Nb₂CT_{x-500}	46.0%	45.1%	5.6%	43.0%	6.3%	0.0%
Nb₂CT_{x-400}	32.8%	61.6%	8.2 %	30.2%	0.0%	0.0%

Table S4. The content of F element and its constituents in each sample in XPS.

sample/content	F 1s	-F	Li-F
Nb₂CT_x	10.6%	100%	0
Li-Nb₂CT_x	4.5%	70.7%	29.4%
Li-Nb₂CT_{x-200}	6.2%	51.0%	49.0%
Li-Nb₂CT_{x-300}	3.5%	74.0%	26.0%
Li-Nb₂CT_{x-400}	2.0%	35.8%	64.3%
Li-Nb₂CT_{x-500}	1.7%	39.3%	60.7%
Nb₂CT_{x-400}	3.1%	100%	0

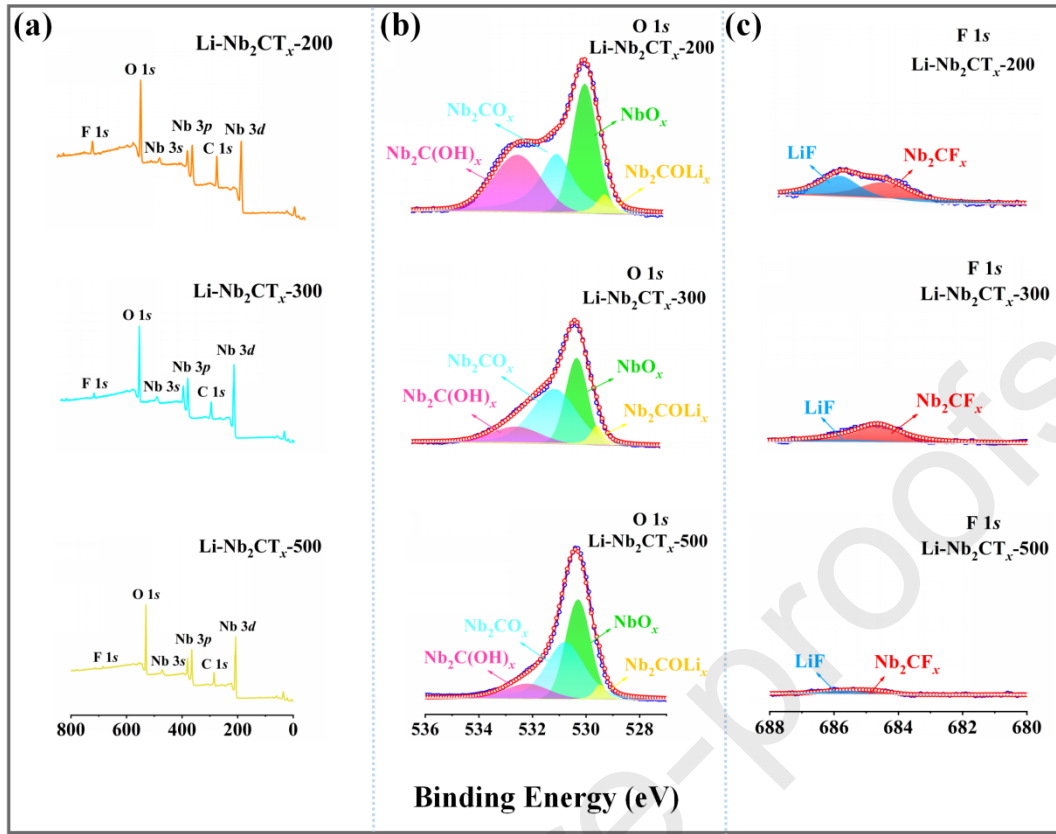


Fig. S1. (a) Survey XPS spectrum, (b) O 1s spectra, (c) F 1s spectra of Li-Nb₂CT_x-200, Li-Nb₂CT_x-300 and Li-Nb₂CT_x-500.

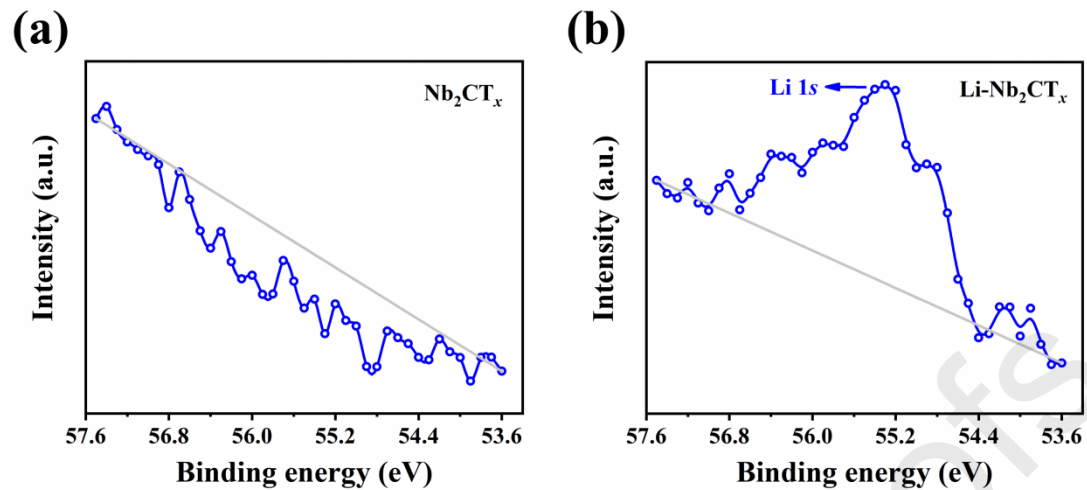


Fig. S2. The Li 1s spectrum of (a) Nb_2CT_x and (b) $\text{Li-Nb}_2\text{CT}_x$ in XPS.

For the Nb_2CT_x , the (002) peak of untreated Nb_2CT_x after 400 °C annealing is shifted to a larger angle with interlayer spacing about 7.62 Å due to the removal of water between layers (Fig. S3a). Meanwhile, the SEM images of untreated Nb_2CT_x annealed at 400 is shown in Fig. S3b, and Nb_2CT_x -400 maintains a good layered structure. O– and F–high resolution spectra are shown in Fig. S3c and d, respectively. The contents of –O[–], –OH and –F functional groups of Nb_2CT_x -400 are 20.2%, 2.7% and 3.1%, respectively. As shown in Fig. S3e, at a current density of 0.05 A g^{–1}, the specific capacity of Nb_2CT_x -400 can reach 257 mAh g^{–1} after 50 cycles. Nb_2CT_x -400 exhibits stable and durable capacity at different current densities (0.05~2A g^{–1}) and decreases steadily as current density increases (Fig. S3f). At the same time, the ultra-long cycle stability of Nb_2CT_x -400 electrode under high current density of 2 A g^{–1} was tested, too. After the ultra-long cycle of 2000 cycle, the specific capacity was maintained at 186 mAh g^{–1} (Fig. S3g).

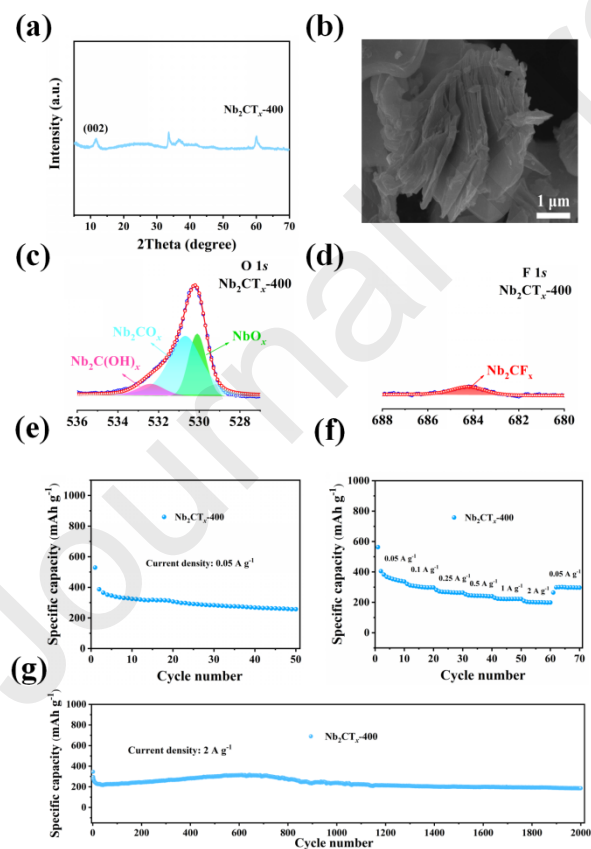


Fig. S3. (a) XRD, (b) SEM, (c) O 1s spectra, (d) F 1s spectra, (e) Cycling properties at 0.05 A g^{–1}, (f) Rate performance and (g) Cycling performance at 2.0 A g^{–1} of Nb_2CT_x -400.

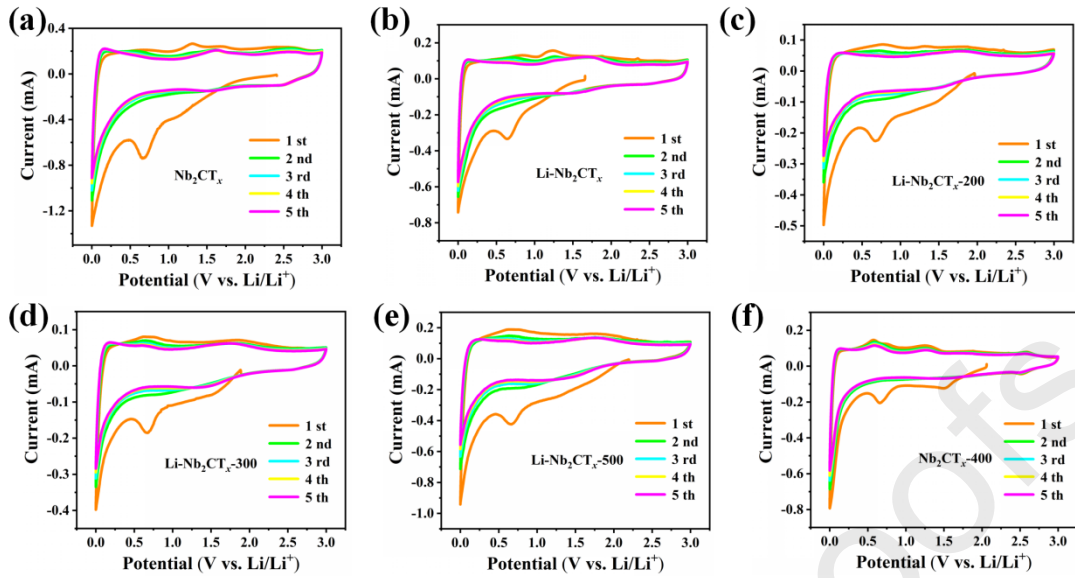


Fig. S4. CV curves of (a) Nb_2CT_x , (b) $\text{Li}-\text{Nb}_2\text{CT}_x$, (c) $\text{Li}-\text{Nb}_2\text{CT}_x-200$, (d) $\text{Li}-\text{Nb}_2\text{CT}_x-300$, (e) $\text{Li}-\text{Nb}_2\text{CT}_x-500$ and (f) $\text{Nb}_2\text{CT}_x-400$ at 0.5 mV s^{-1} .

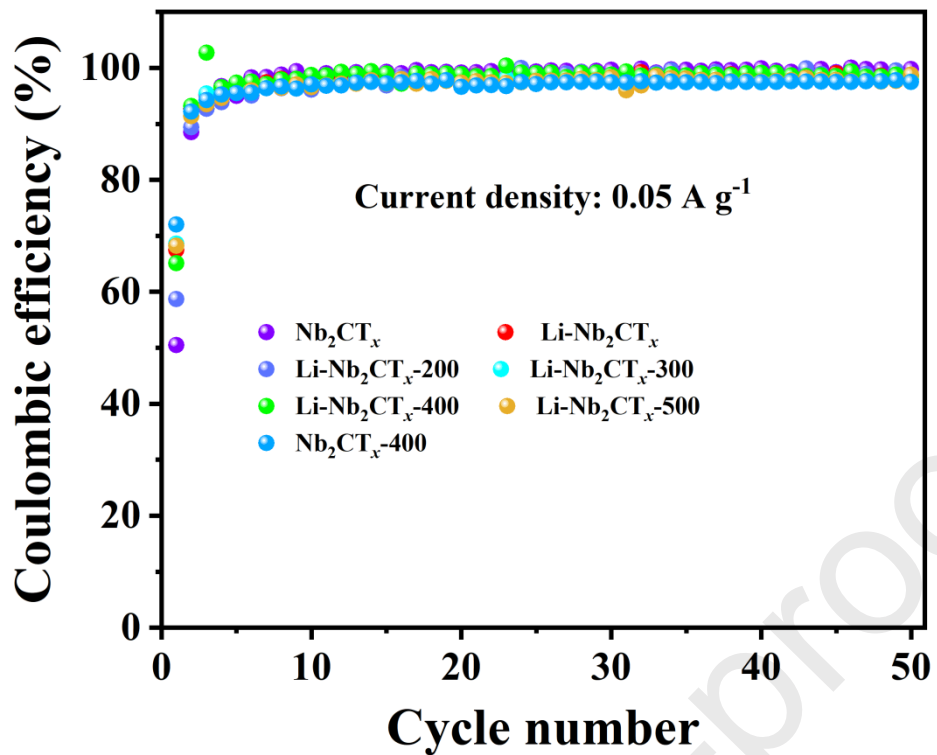


Fig. S5. The corresponding coulombic efficiency of different Nb₂CT_x MXene at 0.05 A g⁻¹.

References

- [1] T.M. Su, R. Peng, Z.D. Hood, M. Naguib, I.N. Ivanov, J.K. Keum, Z.Z. Qin, Z.H. Guo, Z.L. Wu, *ChemSusChem* 11 (2018) 688–699.
- [2] H.R. Byon, B.M. Gallant, S. Woo and Y. Shao-Horn, *Adv. Funct. Mater.* 23 (2013) 1037–1045.
- [3] J. Halim, K.M. Cook, M. Naguib, P. Eklund, Y. Gogotsi, J. Rosen and M.W. Barsoum, *Appl. Surf. Sci.* 362 (2016) 406–417.
- [4] J. Halim, S. Kota, M. R. Lukatskaya, M. Naguib, M. Q. Zhao, E. J. Moon, J. Pitcock, J. Nanda, S. J. May, Y. Gogotsi and M. W. Barsoum, *Adv. Funct. Mater.* 26 (2016) 3118.
- [5] B. Heim, C.N. Taylor, D.M. Zigon, S. O'Dell, J.P. Allain, *Nucl. Instrum. Meth. B.* 269 (2011) 1262–1265.
- [6] Y.D. Agnese, M.R. Lukatskaya, K.M. Cook, P.L. Taberna, Y. Gogotsi, P. Simon, *Electrochem. Commun.* 48 (2014) 118–122.
- [7] P. Niehoff, S. Passerini, M. Winter, *Langmuir* 29 (2013) 5806–5816.

Declaration of interests

The authors declare that they have no known competing financial interests or personal relationships that could have appeared to influence the work reported in this paper.

The authors declare the following financial interests/personal relationships which may be considered as potential competing interests: